



1 **Influence of Bulk Microphysics Schemes upon Weather Research**
2 **and Forecasting (WRF) Version 3.6.1 Nor'easter Simulations**

3 Stephen D. Nicholls^{1,2}, Steven G. Decker³, Wei-Kuo Tao¹, Stephen E. Lang^{1,4}, Jainn J. Shi^{1,5}, and
4 Karen I. Mohr¹

5 ¹NASA-Goddard Space Flight Center, Greenbelt, 20716, United States of America

6 ²Joint Center for Earth Systems Technology, Baltimore, NASA-Goddard Space Flight Center, Baltimore, 21250,
7 United States of America

8 ³Department of Environmental Sciences, Rutgers, The State University of New Jersey, 08850, United States of
9 America

10 ⁴Science Systems and Applications, Inc., Lanham, 20706, United States of America

11 ⁵Goddard Earth Sciences Technology and Research, Morgan State University, 21251, United States of America

12 Correspondence to: Stephen D. Nicholls (stephen.d.nicholls@nasa.gov)



13 **Abstract.** This study evaluated the impact of five, single- or double- moment bulk microphysics schemes (BMPS) on
14 Weather Research and Forecasting (WRF) model (version 3.6.1) winter storm simulations. Model simulations were
15 integrated for 180 hours, starting 72 hours prior to the first measurable precipitation in the highly populated Mid-
16 Atlantic U.S. Simulated precipitation fields were well-matched to precipitation products. However, total
17 accumulations tended to be over biased (1.10–2.10) and exhibited low-to-moderate threat scores (0.27–0.59). Non-
18 frozen hydrometeor species from single-moment BMPS produced similar mixing ratio profiles and maximum
19 saturation levels due to a common parameterization heritage. Greater variability occurred with frozen microphysical
20 species due to varying assumptions among BMPSs regarding ice supersaturation amounts, the dry collection of snow
21 by graupel, various ice collection efficiencies, snow and graupel density and size mappings/intercept parameters, and
22 hydrometeor terminal velocities. The addition of double-moment rain and cloud water resulted in minimal change to
23 species spatial extent or maximum saturation level, however rain mixing ratios tended higher. Although hydrometeor
24 differences varied by up to an order of magnitude among the BMPSs, similarly large variability was not upscaled to
25 mesoscale and synoptic scales.

26 1 Introduction

27 Bulk microphysical parameterization schemes (BMPSs) within numerical weather prediction models have
28 become increasingly complex and computationally expensive. Modern prognostic weather models, such as the
29 Weather Research and Forecasting (WRF) model (Skamarock et al., 2008), offer BMPS options ranging from the
30 simple, warm rain only Kessler scheme (Kessler, 1969) to the full, double-moment, six-class Morrison scheme
31 (Morrison et al., 2009). Microphysics parameterizations (along with cumulus parameterizations) drive cloud and
32 precipitation processes and have far reaching consequences within numerical weather simulations (radiation, moisture,
33 aerosols, *etc.*). Given its importance for simulations, Tao et al. (2011) noted at least 36 major, published, microphysics-
34 focused studies primarily in the context of idealized simulations, hurricanes, and mid-latitude convection. More
35 recently, the observational studies of Stark (2012) and Ganetis and Colle (2015) investigated microphysical species
36 variability within East Coast U.S. winter storms (locally called “nor’easters”) and have underscored the need to
37 investigate how microphysical parameterizations alter simulations of these powerful cyclones, which is the objective
38 of the present work.

39 A “nor’easter” is a large (~2000 km), mid-latitude cyclone occurring between October and April and is capable
40 of bringing punishing winds, copious precipitation, and potential coastal flooding to the Northeastern U.S. (Kocin and
41 Uccellini 2004; Jacobs et al., 2005; Ashton et al., 2008). To illustrate their potential severity, ten strong December
42 nor’easter events between 1980 and 2011 resulted in 29.3 billion U.S. dollars in associated damages (Smith and Katz,
43 2013). Such damages are possible given the high economic output (16 billion U.S. dollars per day) of the northeastern
44 U.S. (Morath, 2016). Given their importance to prognostic weather and climate models, this study aims to evaluate
45 how BMPSs within WRF impacts its simulations of nor’easter development, the storm environment, and precipitation.

46 Recent nor’easter studies are scarce in light of extensive research conducted on these cyclones, primarily during
47 the 1980s, which addressed key drivers including frontogenesis and baroclinicity (Bosart, 1981; Forbes et al., 1987;



48 Stauffer and Warner, 1987), anticyclones (Uccellini and Kocin, 1987), latent heat release (Uccellini et al., 1987), and
49 moisture transport by the low-level jet (Uccellini and Kocin, 1987; Mailhot and Chouinard, 1989). Despite extensive
50 observational analyses, there is much less work on nor'easter and winter storm simulations in general, particularly
51 those related to BMPSs.

52 Reisner et al. (1998) ran several single and double-moment BMPS Mesoscale Model Version 5 simulations of
53 winter storms impacting the Colorado Front Range for the Winter Icing and Storms Project. Double moment-based
54 simulations produced more accurate simulations of supercooled water and ice mixing ratios than those from single-
55 moment schemes. However, single moment-based results vastly improved when snow-size distribution intercepts were
56 derived from a diagnostic equation rather than set as a fixed value.

57 Wu and Pretty (2010) investigated how five, six-class BMPSs affected WRF simulations of four polar-low events
58 (two over Japan, two over the Nordic Sea). Their simulations yielded nearly identical storm tracks, yet had notable
59 differences in cloud top temperature and precipitation field errors. In this study, the WRF single-moment BMPS (Hong
60 and Lim, 2006) produced marginally superior simulations of cloud and precipitation processes as compared to other
61 schemes. For warmer, tropical cyclones, Tao et al. (2011) investigated how four, six-class BMPSs impacted WRF
62 simulations of Hurricane Katrina and demonstrated that BMPS choice had a minimal impact upon storm track.
63 However, variations in sea-level pressure (SLP) were considerably higher (up to 50 hPa).

64 Shi et al. (2010) evaluated several WRF single-moment BMPSs for a lake-effect snow and a 20-22 January 2007
65 synoptic event. Simulated radar reflectivity and cloud top temperature validation revealed WRF accurately simulated
66 event onset and termination times, cloud coverage, and lake-effect snow band extent. However, simulated station
67 snowfall rates were less accurate due to error in predicting exact points within a mesoscale grid. WRF-simulated snow
68 bands showed minimal BMPS-based differences because cold temperatures and weak vertical velocities prevented
69 graupel generation in all simulations. A more recent lake-effect snow modeling study by Reeves and Dawson (2013)
70 investigated WRF sensitivity to eight different BMPSs during a December 2009 event. Their study found precipitation
71 rate and its coverage were highly sensitive to BMPS because in half of their simulations vertical velocities exceeded
72 hydrometeor terminal fall speeds which prolonged hydrometeor residence times. Terminal fall speeds differences
73 existed due to varying assumptions associated with frozen hydrometeor species (i.e., snow density values,
74 temperature-dependent snow intercept values, and graupel generation terms).

75 In a similar spirit to previous studies, this work will test WRF nor'easter simulation sensitivity to six- and seven-
76 class BMPSs and focus on storm and microphysical properties, precipitation, and the simulated storm environment.
77 The remainder of this paper is divided into three sections. Section 2 explains the methodology and analysis methods.
78 Section 3 shows the results. Finally section 4 describes the conclusions, its implications, and prospects for future
79 research.

80 **2 Methods**

81 **2.1 Study design**



82 We utilized WRF version 3.6.1 (hereafter W361) which solves fully-compressible, non-hydrostatic, Eulerian
83 equations in terrain-following coordinates (Skamarock et al., 2008). There was a four-domain, convection-resolving
84 WRF grid (Fig. 1) with two-way feedback. It had 45-, 15-, 5-, and 1.667-km grid spacing, 61 vertical levels, and a 50-
85 hPa (~20 km) model top. Boundary conditions were derived from $1^\circ \times 1^\circ$ resolution Global Forecasting System model
86 operational analysis (GMA) data. Except for a fourth domain, this model configuration and the following
87 parameterizations were successfully applied in a previous nor'easter study (Nicholls and Decker, 2015) and was
88 consistent with past and present WRF model studies at NASA-Goddard Space Flight Center (i.e., Shi et al., 2010; Tao
89 et al. 2011). Model parameterizations include:

- 90 ▪ Longwave radiation: New Goddard Scheme (Chou and Suarez, 1999; Chou and Suarez, 2001)
- 91 ▪ Shortwave radiation: New Goddard Scheme (Chou and Suarez, 1999)
- 92 ▪ Surface layer: Eta similarity (Monin and Obukhov, 1954; Janjic, 2002)
- 93 ▪ Land surface: NOAH (Chen and Dudhia, 2001)
- 94 ▪ Boundary layer: Mellor-Yamada-Janjic (Mellor and Yamada 1982; Janjic 2002)
- 95 ▪ Cumulus parameterization: Kain-Fritsch (Kain, 2004) (Not applied to domains 3 and 4)

96 This study investigates the same, diverse, selectively chosen sample of seven nor'easter cases from Nicholls and
97 Decker (2015) which vary in both severity and time of year (Table 1). Nor'easter events in Table 1 list one case for
98 each month in which nor'easters occur (October–March) to determine any seasonal dependence or biases, and they
99 are sorted by month rather than chronological order. In Table 1, the Northeast Snowfall Impact Scale (NESIS) value
100 serves as proxy for storm severity (1 is notable and 5 extreme) and is based upon the population impacted, area
101 affected, and snowfall severity (Kocin and Uccellini, 2004). Early and late season storms (Cases 1, 2, and 7) did not
102 have snow and thus do not have a NESIS rating.

103 Simulations are integrated for 180 hours, starting 72 hours prior to the first precipitation impacts in the highly
104 populated Mid-Atlantic region. This lead time allows for sufficient model spin-up time, establishment of the coastal
105 baroclinic zone, and surface latent heat flux generation which are crucial components for nor'easter development
106 (Bosart, 1981; Uccellini and Kocin, 1987; Kuo et al., 1991; Mote et al., 1997; Kocin and Uccellini, 2004; Yao et al.,
107 2008). We define the first precipitation impact time as the first 0.5 mm (~0.02 inch) precipitation reading from the
108 New Jersey Weather and Climate Network (D. A. Robinson, pre-print, 2005). A smaller threshold is not used to avoid
109 capturing isolated showers well ahead of the primary precipitation shield. A New Jersey-centric approach was chosen
110 due to its high population density (461.6 / km²), significant contribution (\$473 billion) to the U.S. gross domestic
111 product, and its central location in the Mid-Atlantic (United States Census Bureau, unpublished data, 2012).

112 To investigate BMPS influence upon W361 nor'easter simulations, five BMPS are used (Table 2). As shown in
113 Table 2, the selected schemes include three, six-class, three-ice, single-moment schemes Lin (Lin6; Lin et al., 1983;
114 Rutledge and Hobbs, 1984), Goddard Cumulus Ensemble (GCE6; Tao et al., 1989; Lang et al., 2007), and WRF single
115 moment (WSM6; Hong and Lim 2006), a seven-class, four-ice, single-moment scheme (GCE7; Lang et al. 2014), and
116 finally, a six-class, three-ice, double-moment scheme (WRF double-moment, six class (WDM6; Lim and Hong
117 2010)). For this study, all five BMPSs were each run for the nor'easter events listed in Table 1.



118 2.2 Verification and analysis techniques

119 Model output was evaluated against both GMA and 4-km resolution Stage IV precipitation data (Y. Lin and K.E.
120 Mitchell, preprints, 2005). GMA data validated all model output (except precipitation) due to its extensive coverage,
121 and lack of available in-situ data in data-sparse regions. Stage IV is a six-hourly, gridded precipitation product derived
122 from rain gauge and radar data with 4-km spatial resolution. Prior to any validation, all data were interpolated to the
123 coarsest grid spacing.

124 Model output analysis consisted of several parts. Nor'easter storm tracks were derived via an objective, self-coded
125 algorithm similar to that used at the Climate Prediction Center (Serreze, 1995; Serreze et al., 1997). At each storm
126 position, minimum SLP (MSLP), maximum wind speed, and track error were stored and compared to model analysis.
127 Precipitation values and their distribution were evaluated against Stage IV data and validated using bias and threat
128 score (critical success index) calculations (Wilks, 2011). The simulated hydrometeor species analysis was comprised
129 of two parts: precipitable mixing ratios, and composite mixing ratio profiles. Precipitable mixing ratio is derived from
130 the equation for precipitable water and is defined as the following:

$$131 \quad PMR = \frac{1}{\rho g} \int_{p_{top}}^{p_{sfc}} w \, dp \quad (1)$$

132 In Eq. (1), PMR is the precipitable mixing ratio in m, ρ is the density of water (1000 kg m^{-3}); g is the gravitational
133 constant (9.8 m s^{-2}); p_{sfc} is the surface pressure (Pa), p_{top} is the model top pressure (Pa); w is the mixing ratio (kg kg^{-1});
134 dp is the change in atmospheric pressure between model levels (Pa). Composite mixing ratio profiles were
135 calculated within a 600-km wide cubic volume centered at both model- and GMA-relative surface cyclone locations
136 (hereafter, model-relative and GMA-relative storm environments, respectively). For illustrative purposes, the red,
137 dashed box in Figure 2, panel 1 denotes the GMA-relative storm environment extent at 12 UTC 15 October 2009.
138 Finally, the accuracy of model- and GMA-relative storm environment WRF simulations will be validated using the
139 non-hydrostatic, moist, total energy norm (Kim and Jung, 2009). Energy norm integrations were capped at $\sim 100 \text{ hPa}$
140 to limit large temperature errors near the model top and calculated using Eq. (2).

$$141 \quad E_m = \iiint_{\sigma, x, y} \frac{1}{2} \left[u'^2 + v'^2 + w'^2 + \left(\frac{g}{N_r \theta_r} \right)^2 \theta'^2 + \left(\frac{1}{\rho_r c_s} \right)^2 p'^2 + \omega_q \frac{L^2}{c_p T_r} q'^2 \right] dy \, dx \, d\sigma \quad (2)$$

142 In Eq. (2), E_m is the moist total energy norm ($\text{J m}^2 \text{ kg}^{-1}$); u' , v' , and w' are the zonal, meridional, and vertical wind
143 perturbations (m s^{-1}), respectively; p' is the pressure perturbation (Pa); θ' is the potential temperature perturbation (K);
144 q' is the mixing ratio perturbation (kg kg^{-1}). N_r , θ_r , ρ_r , T_r , and c_s are the reference Brunt Väisälä frequency (0.0124 s^{-1}),
145 reference potential temperature (270 K), reference air density (1.27 kg m^{-3}), reference air temperature (270 K), and
146 speed of sound (329.31 m s^{-1}), respectively. Finally, c_p is the specific heat at constant pressure ($1005 \text{ J kg}^{-1} \text{ K}^{-1}$) and
147 ω_q is a scaling factor (0.1). Finally, y , x , and σ , denote the zonal, meridional, and sigma (terrain following) directional
148 components, respectively. Our analysis focus on the energy norm was influenced by Buizza et al. (2005), who made
149 a compelling case for its usage at ECMWF for model validation given its total model volume integration, lack of
150 single-layer sensitivity, and inclusion of temperature, wind, pressure, and moisture errors. Similar to root mean square
151 error, smaller values denote less error.



152 3. Results

153 3.1 Nor'easter track and property analysis

154 Figure 2 displays storm tracks from W361 BMPS simulations (colors) and GMA (black), and Fig. 3 shows GMA-
155 relative track errors for all seven cases. In Fig. 3, smaller, colored symbols denote six-hourly track error, whereas the
156 larger, black symbols denote the model mean. Similar to Wu and Petty (2010) and Tao et al. (2011), BMPS choice
157 yields modest storm track changes (Δ BMPS average; 84 km) and no apparent directional biases among the schemes.
158 As compared to GMA, six-hourly storm track errors vary greatly ranging from 30 km (GCE6, Case 6) to 1,594 km
159 (GCE7, Case 2). Nor'easters with less track error (Case 3, 4, and 6) formed within a regions of stronger differential
160 cyclonic vorticity advection (CVA) aloft, whereas for higher track error cases (Cases 2 and 7) CVA was far weaker
161 (not shown). To quantify case-to-case track errors, Table 3 lists average track errors for each case, using bold type for
162 large errors (> 400 km). Both Table 3 and Fig. 3 indicate that the GCE6-based simulations have the least average track
163 error in four out of seven cases (Cases 1, 3, 4, and 6) and overall (406 km). However, this conclusion is not definitive,
164 given a 187 km maximum track error spread (Case 1, WSM6-GCE6) among BMPSs.

165 In addition to average track errors, Table 3 also contains other key nor'easter properties including MSLP,
166 maximum MSLP deepening rate, and maximum wind speed within the model-relative storm environment. To
167 supplement Table 3, Fig. 4 displays six-hourly MSLP and maximum 10 m wind speeds from all W361 runs and GMA
168 for Cases 2, 3, 4, and 5. These cases have the least and greatest average track errors (See Table 3). In Table 3, large
169 deviations from GMA are in bold type (Δ MSLP > 5 hPa, Δ deepening rate > 5 hPa / 6 hours, and Δ 10 m winds > 5
170 m s^{-1}). Consistent with the storm track analysis, Case 2 has notable deviations in both MSLP (up to 8.6 hPa) and 10 m
171 winds (up to 7.1 m s^{-1}). Large track errors however are not required for MSLP and wind speed errors to be large. The
172 highest MSLP errors originate from Cases 3 (10.5 hPa; Lin6) and 4 (9.3 hPa; Lin6) and are statistically significant in
173 the former (maximum p-value 0.032, GCE6). Although sizable, these MSLP differences fall well short of the 50-hPa
174 MSLP differences cited in Tao et al. (2011) possibly due to the less extreme MSLP values associated with nor'easters
175 as compared to hurricanes. Consistency between BMPSs simulations in Fig. 1, Fig. 4, and Table 3 suggests that
176 nor'easter MSLP and wind errors are more associated with differences in steering flow and cyclonic vorticity
177 advection aloft rather than BMPS selection. Case 3 best illustrates this hypothesis as MSLP lags notably behind GMA
178 starting when all simulations diverged from GMA on December 19 (See Figs. 1 and 4), yet once the secondary low
179 developed further north along the Gulf Stream, latent heat fluxes increase greatly ($> 1000 \text{ W m}^{-2}$) and the MSLP gap
180 in Fig. 4 closes considerably. A similar situation occurs in Case 2, where 10 m maximum winds became far stronger
181 ($> 10 \text{ m s}^{-1}$) in GMA than in W361 simulations. Stronger winds exist in GMA than W361 simulations because its
182 cyclone remains over the strong baroclinic zone associated with the Gulf Stream, rather than the more energy-poor
183 inland track exhibited by all W361 simulations track (See Fig. 2, panel 2).

184 3.2 Stage IV precipitation analysis

185 One of the most crippling potential impacts associated with nor'easters comes from precipitation, which is
186 partially driven in simulations by BMPSs. To demonstrate any potential BMPS sensitivity, Fig. 5 displays 72-hour



187 precipitation accumulations (forecast hours 48–120) from Stage IV and Lin6 (top panels), differences between the
188 remaining BMPSs and Lin6 (middle panels), and finally precipitation probability density and cumulative distribution
189 functions (PDF and CDF, respectively) from Cases 4 and 6. These two cases have the lowest track errors in Table 3
190 which facilitated easier comparisons to Stage IV precipitation data. Table 4 contains bias and threat scores values from
191 all seven cases assuming a 12.5 mm to quantify simulated precipitation field accuracy and tendency.

192 Threat score and bias values in Table 4 indicate Cases 2 and 3 to be clear outliers given bias scores exceeding 4
193 and less than 1, respectively. These outlier values result from the spatial limitations of the Stage IV product due to its
194 reliance upon radar and rain gauge data. In Cases 2 and 3, either the GMA or W361 simulated cyclone crossed the
195 data cut-off region prematurely resulting in a severe over-bias (4.50–4.72) and an under-bias (0.71–0.85), respectively.
196 For the remaining five nor'easter cases, Table 4 indicates low (0.29, GCE7, Case 7) to moderate (0.59, WDM6, Case
197 6) threat scores and over-biased precipitation totals (bias range: 1.10–2.10). Although case-to-case threat score and
198 bias vary up to 0.27 and 0.98, inter-BMPS threat scores and biases (except Case 4) are an order of magnitude smaller.
199 Consistent with Hong et al. (2010), threat score and bias values for WSM6 are equal to or improved upon by WDM6
200 due to its inclusion of a cloud condensation nuclei (CCN) feedback. Overall, despite being the simplest BPMS tested,
201 Lin6 did manage marginally better threat scores in three of the five nor'easter events and has the lowest overall average
202 bias.

203 As Fig. 4 illustrates, Case 4 W361 simulations produce a precipitation extent similar to Stage IV (except off
204 Georgia), yet exact precipitation totals along the coast are too high. Case 6 exhibits similar behavior and has well-
205 matched extent, but excessive precipitation totals. Precipitation PDF and CDFs show three distinctive bin categories:
206 5–10 mm, 10–55 mm, and 55 mm+. The strong-convection modeling studies of Ridout et al. (2005) and Dravitzki and
207 McGregor (2011) found both GFS and Coupled Ocean/Atmosphere Mesoscale Prediction System (COAMPS)
208 produced too much light precipitation and too much heavy precipitation. Given WRF's common heritage with GFS,
209 similar precipitation biases would be expected. However, two nor'easter cases (Cases 6 and 7) deviate from this
210 expectation and generated too little light precipitation (5–10 mm) and too much heavier precipitation (10–55 mm).
211 Once above 55 mm, all cases produce too much precipitation. These findings likely stem from two sources: different
212 Stage IV domain exit times and the focus in previous studies on convective rather than stratiform events, which may
213 lead to differences in simulated precipitation generation. Marginal changes in QPF (< 15 mm) and threat scores
214 between the BMPS W361 runs are consistent with Fritsch and Carbone (2004) and Wang and Clark (2010) who
215 evaluated the accuracy of simulated precipitation in warm-season events and quasi-stationary fronts, respectively.

216 3.3 Hydrometeor species analysis

217 Figure 6 displays precipitable mixing ratios for six microphysics species (water vapor, cloud water, graupel, cloud
218 ice, rain, and snow) at 18 UTC 26 January 2015 over the entirety of Domain 3. This time is selected for its
219 exceptionally small track error (< 50 km) and because all simulated cyclones are located within the 5-km Domain 3
220 and 1.667-km Domain 4. Figure 6 depicts precipitable mixing ratios rather than column-integrated mixing ratios as it
221 is easier to express these data as a height (mm) than as a weight (kg m^{-2}). Hail is excluded as it is specific to GCE7
222 and is an order of magnitude less (on average) than the other hydrometeor species. Figure 6 shows most precipitable



223 mixing ratio species (especially cloud ice and snow) vary considerably among BMPSs though there are identifiable
224 trends due to the underlying assumptions made within the BMPS as explained in more detail below. Figure 7 shows
225 Case 4, domain 3, composite hydrometeor mixing ratio values averaged from the model-relative storm environments
226 of each W361 BMPS simulation. The first five panels exclude water vapor (two orders of magnitude larger), but do
227 include composite vertical velocity as a black, solid line. Composite water vapor mixing ratios are shown for all W361
228 simulations in the last panel of Fig. 7. Only water vapor can be validated because the other species are nonexistent in
229 GMA and ground and space validation microphysical data are lacking, especially over the data-poor North Atlantic
230 (Li et al., 2008; Lebsock and Su, 2014).

231 All BMPSs share a common heritage in the Lin6 scheme. With the exception of the two-moment cloud water and
232 rain and CCN-cloud droplet feedbacks in WDM6, the BMPSs differ primarily in how each addresses frozen
233 hydrometeor species (cloud ice, graupel, and snow). Their common programming heritage is evident from the nearly
234 identical (exception: WDM6) rain mixing ratio profiles (Fig. 7), saturation heights (Fig. 7), and precipitable rain fields
235 (Fig. 6) and is consistent with Wu and Petty (2010). WDM6 varies from the other single-moment BMPSs because
236 CCN, rain and cloud water are forecasted rather than diagnosed from derivative equations (Hong et al., 2010). While
237 such changes have minimal impact upon maximum saturation heights or the precipitable rain coverage area, maximum
238 rain mixing ratio values are noticeably higher aloft and decrease sharply towards the surface.

239 Similar to rain mixing ratios, cloud water mixing ratios exhibit little variability in either the precipitable cloud
240 water extent (Fig. 6) or the maximum saturation level (Fig. 7), but maximum mixing ratio values vary even between
241 single-moment schemes. Differing allowances in the amount of ice supersaturation between GCE7 (Chern et al. 2016)
242 and WSM6 (Hong et al. 2010) are likely to account for the differences in the maximum cloud water mixing ratios.
243 Although in WDM6 cloud water is double-moment, which allows the number concentrations to vary, in this instance,
244 the maximum mixing ratios are only decreased slightly relative to WSM6. Small variations in cloud water between
245 WSM6 and WDM6 suggest cloud water number concentrations in WDM6 are potentially close to the assumed 300
246 cm^{-3} number concentration in WSM6 (Hong et al. 2010) and/or the larger-scale environment/forcing is a dominant
247 factor as water supersaturation is negligible.

248 Among the BMPSs, Figs. 6 and 7 show that precipitable snow and snow mixing ratios vary considerably with
249 Lin6 having the smallest and GCE6 the largest amounts. Dudhia et al. (2008) and Tao et al. (2011) associate the
250 dearth of snow in Lin6 to its high rates of dry collection by graupel, low snow size distribution intercept (decreased
251 surface area), and auto-conversion of snow to either graupel or hail at high mixing ratios. In GCE6, dry collection of
252 snow and ice by graupel is turned off and results in a large increase in snow at the expense of graupel (Lang et al.
253 2007). Although the snow riming efficiency was reduced, the omission of dry collection along with and the continued
254 assumption of water saturation for the vapor growth of cloud ice to snow contributes to its high snow-mixing ratios
255 (Reeves and Dawson, 2013; Lang et al. 2014). In GCE7, this latter issue has been addressed and along with numerous
256 other changes, including the introduction and of a snow size and density mapping, snow breakup interactions, and a
257 new vertical-velocity-dependent ice super saturation assumption (Lang et al., 2007; Lang et al., 2011; Lang et al.,
258 2014; Chern et al., 2016; Tao et al., 2016). Figures 6 and 7 show that although the combination of an RH correction
259 factor (Lang et al., 2011) in conjunction with the new ice super saturation adjustment (Tao et al., 2016) reduce the



260 efficiency of vapor growth of cloud ice to snow, the new snow mapping and enhanced cloud ice to snow auto-
261 conversion in GCE7 help to keep snow mixing ratios higher than in non-GCE BMPSSs. Unlike Lin6, WSM6 and
262 WDM6 graupel and snow fall speeds are assumed to be identical within a grid cell (Dudhia et al., 2008) and the ice
263 nuclei concentration is a function of temperature (Hong et al., 2008). These two changes effectively eliminated the
264 accretion of snow by graupel and increased snow mixing ratios at colder temperatures (Dudhia et al., 2008; Hong et
265 al., 2008). Figure 7 shows that the level of maximum snow content is largely conserved across the BMPSSs, except
266 for Lin6, which is 100 hPa lower as differential snow and graupel fall speeds allow graupel to collect snow.

267 Maximum mean graupel mixing ratios in the column are generally much less than for snow except for Lin6 where
268 dry collection aloft is dominated by graupel and is unrealistic (Stith et al., 2002). In contrast, GCE7 produces the most
269 snow and the least amount of graupel. GCE7 includes a graupel size mapping, but the combination of the snow size
270 mapping, which generally decreases snow sizes aloft (thus increasing their surface area and vapor growth), the addition
271 of deposition conversion processes wherein graupel/hail particles experiencing deposition growth at colder
272 temperatures are converted to snow, and changes to the cloud ice that lead to more cloud ice and less super-cooled
273 cloud water (see below) and thus reduced riming, favor snow over graupel even more (Lang et al. 2014; Chern et al.,
274 2016; Tao et al., 2016). Consistent with Reeves and Dawson (2013), graupel mixing ratios are around 30-50 % that
275 of snow for WSM6 and WDM6. Despite having a smaller peak mean graupel mixing ratio in the column (Fig. 7),
276 WDM6 produces locally enhanced precipitable graupel values in Fig. 6 relative to WSM6.

277 Although up to ninety percent smaller in magnitude than snow (GCE6), cloud ice mixing ratios vary greatly
278 amongst the BMPSSs in Figs. 6 and 7. They are highest in GCE7 and lowest in Lin6. Wu and Petty (2010) similarly
279 found low cloud ice mixing ratios from their Lin6 simulations and ascribed it to dry collection by graupel, lack of an
280 ice sedimentation term, and fixed cloud-ice size distribution. Similar to Lin6, in GCE6 the cloud-ice size distribution
281 is monodispersed, but as noted in Lang et al. (2011) and Tao et al. (2016), the vapor growth of cloud ice to snow in
282 GCE6 was still based upon an assumed water saturation, which made this term too efficient and helped keep cloud ice
283 mixing ratios lower. This term includes an RH correction factor in GCE7, which depends upon the amount of ice
284 supersaturation, which in turn is dependent on the vertical velocity in GCE7. These factors effectively blunt this term's
285 over-efficiency. Additionally, in GCE7, contact and immersion freezing terms are included (Lang et al., 2011), cloud
286 ice collection by snow efficiency is a function of snow size (Lang et al., 2011; Lang et al., 2014), there is a maximum
287 limit on cloud ice particle size (Tao et al., 2016), the ice nuclei concentration follows the Cooper curve (Cooper, 1986;
288 Tao et al., 2016), and cloud ice can persist even in ice subsaturated conditions (i.e., when RH values for ice are greater
289 than or equal to 70 %) (Lang et al., 2011; Lang et al., 2014). Despite the increased cloud ice-to-snow auto conversion
290 (Lang et al. 2014; Tao et al. 2016), these changes combine to produce almost 100 % more cloud ice in GCE7 than in
291 GCE6 (See Fig. 7). Similar to GCE7, WSM6 runs generate larger cloud ice mixing ratios than Lin6, which Wu and
292 Petty (2010) attribute to excess cloud glaciation at temperatures between 0°C and -20°C and its usage of fixed cloud
293 ice size intercepts. Additionally, both WSM6 and WDM6 also include ice sedimentation terms (Hong et al., 2008).
294 Despite the differences in the cloud ice mixing ratio amounts, the level of maximum mean cloud ice mixing ratio is
295 around 300 hPa for all of the BMPSSs.



296 Neither precipitable mixing ratio nor vertical velocity exhibit notable sensitivity to the BMPSs despite the above
297 hydrometeor results. Close inspection of Fig. 7 reveals that GMA water vapor mixing ratios are slightly higher below
298 800 hPa on average than those from the W361 BMPS simulations and slightly lower above that level, while Fig. 6
299 hints at a potential small dry bias in WRF. Although one order of magnitude or more smaller than water vapor mixing
300 ratios, slight differences in the other hydrometeor species (notably cloud ice and snow) act to drain the available
301 moisture (GCE7 versus Lin6) at slightly different rates. In contrast to Reeves and Dawson (2013), model-relative
302 vertical velocities in nor'easters extend through the depth of the troposphere, whereas for lake-effect snow, positive
303 vertical velocities may only extend to 700 hPa. Enhanced vertical velocities above 770 hPa are driven primarily by
304 isentropic lift associated with the warm-conveyor belt (Kocin and Uccellini, 2004)

305 3.4 Energy norm-based analysis of model- and GMA-relative storm environments

306 Figure 8 displays the model-relative storm environment fully-integrated Lin6 energy norm with time (black) and
307 the percent difference between the Lin6 energy norm and all other BMPSs for all seven cases. Lin6 energy norm
308 values provide a fixed reference to inter-compare WRF simulation accuracy because both a WRF and GMA data are
309 used to calculate energy norm values. Figure 9 shows the similar information to Fig. 8, except the energy norm is
310 integrated at each model level and averaged in time. To complement these two figures, Fig. 10 depicts the model-
311 relative time-averaged total energy norm (black) and its six component parts integrated for each level for cases 1, 2,
312 4, and 7 from Lin6, GCE7, and WDM6. Table 5 summarizes the energy norm results for both the model- and GMA-
313 relative storm environments. Given the similar appearance between the GMA- and model-relative storm environment
314 plots (similar shape, slightly different magnitude), we elected to only show model-relative energy norm plots in this
315 section.

316 Closer observation of Figs. 3, 8, and 9 reveal energy norm variability has strong links to both storm track
317 uncertainty (e.g., Fig. 8, Case 7, GCE6) and the energy norm magnitude (e.g., Fig. 9, Case 1, GCE7), yet track errors
318 need not be large to have higher energy norms (i.e., Case 3). Energy norm differences in Fig. 8 vary from 95 % (Case
319 3, GCE7) to -39 % (Case 4, WDM6) where positive percentage values denote higher energy norms than Lin6.
320 Similarly, time-averaged energy norms in Fig. 9 show a slightly smaller range between -24 % (Case 1, WDM6) and
321 79 % (Case 1, GCE7)). Overall, Figs. 8 and 9 show that no one BMPS scheme consistently outperforms the other four
322 schemes, a result quantified in Table 5. In Table 5, the Lin6 scheme has the highest tendency for the lowest energy
323 norm values, but its energy norms are lowest only in 18 out of 62 times (29 %) and 24 out of 67 times (35.8 %) and
324 for 3 out of 7 cases in the model- and GMA-relative storm environments, respectively. There was no statistically
325 significant differences between Lin6 and other BMPSs in two-tailed T-Tests (min p-value: 0.206 (GCE7, Case 1))
326 with the exception of the GCE schemes from Case 7. For this case and these BMPSs, statistical significance is only
327 achieved due to highly variable storm track errors at the last three analysis times when differential CVA aloft was
328 fairly weak. Complicating the energy norm results, WDM6 has the least average error in the GMA-relative storm
329 environment which only makes drawing a decisive conclusion more difficult.

330 Although we could not detect a clearly preferable BMPS for WRF nor'easter simulations, the Figs. 9 and 10 can
331 help diagnose key sources of error. For Cases 1, 2, 4, and 7 (also true for the remaining 3 cases), model-relative storm



332 environment total energy norms are highest near the surface and decrease until the tropopause. Figure 10 shows the
333 total energy norm to be dominated by its temperature and horizontal wind components. By comparing the magnitude
334 of these errors between BMPSSs, it is possible to diagnose that GCE7 has a less accurate depiction of the low-level jet
335 given its higher horizontal wind energy norm values at 858 hPa than as represented by Lin6. Alternatively higher
336 meridional wind errors at and above 500 hPa for GCE7, Case 7, indicate errors in the speed or location of the warm-
337 conveyor belt.

338 4 Conclusions

339 The role and impact of five BMPSSs upon seven, W361 nor'easter simulations is investigated and validated against
340 GMA and the Stage IV precipitation product. Tested BMPSSs include four single-moment (Lin6, GCE6, GCE7, and
341 WSM6) and one double-moment BMPSSs (WDM6). Consistent with previous studies, storm track, MSLP, and
342 maximum 10 m winds exhibits only a minor dependence upon BMPSS with up to 187 km, 7.0 hPa, and 7.6 m s⁻¹ of
343 error variability between BMPSSs, respectively. Relative to GMA, model track errors average 406 km and MSLP and
344 maximum 10 m winds vary up to 10.5 hPa, and 11.2 m s⁻¹ and are only statistically significant when storm track errors
345 involve the Gulf Stream (e.g., Case 3).

346 Simulated precipitation fields exhibit low-to-moderate (0.27–0.59) threat score skill and varying degrees of over-
347 bias (1.10–2.10) when compared to the Stage IV precipitation product. Although most cases generate too much light
348 precipitation and too little heavy precipitation (up to 55 mm) as in previous studies (Ridout et al., 2005; Dravitzki and
349 McGregor, 2011), two cases (6 and 7) reverse this trend. At notably high precipitation accumulation (55 mm+) all
350 BMPSSs generate excessive precipitation (relative to Stage IV). These digressions from previous studies are potentially
351 related to the general lack of strong convection in nor'easters, whereas in previous studies their foci lie on strong-
352 convective events (e.g., hurricanes and squall lines), but validating this claim would require investigation beyond the
353 scope of the present work.

354 Simulated hydrometeor mixing ratios show general similarities for non-frozen hydrometeor species (cloud water
355 and rain) due to their common Lin6 heritage. However, frozen hydrometeor species (snow, graupel, cloud ice)
356 demonstrate considerably larger variability between BMPSSs. Larger changes exist for frozen species due to different
357 assumptions about snow and graupel intercepts, degree of allowable ice supersaturation, snow and graupel density
358 maps, and terminal velocities made by each BMPSS. Despite the increased complexity of WDM6, it did not produce
359 vastly different results from the single-moment BMPSSs. The Lin6 hydrometeor species vary the most relative to other
360 schemes, especially graupel and snow, due to its low snow size intercept and its snow-to-graupel conversion rates.
361 Validations of hydrometeor species (except water vapor) were not performed due to lack of either sufficient radar
362 coverage off the U.S. East Coast or a high-quality, satellite-based hydrometeor product covering all major species
363 (excluding hail).

364 Model and GMA-relative storm environment energy norms indicate that with the exception of Case 7 (due to
365 track error at three times), combined temperature, wind, pressure, and moisture errors failed to yield statistically
366 significant differences (min p-value: 0.206) attributable to BMPSS option. These differences, although not statistically



367 significant do show the Lin6 simulations produce the lowest energy norm in 29 % and 35.8 % of all evaluated model-
368 and GMA-evaluated storm track positions. Energy norms from the remaining BMPSs did not frequently stray more
369 than 20 % from the Lin6 scheme and demonstrated that the greatest contributions to the energy norm were horizontal
370 winds and temperature in the lower troposphere (especially between 850 and 500 hPa). Energy norm results also show
371 that although hydrometeor species mixing ratios varied up to an order of magnitude (snow, Lin6 vs all others), these
372 large changes were not upscaled to mesoscale and synoptic scales.

373 Although none of these results proved definitive, they do strike a cautionary note where higher computational
374 costs associated with double-moment or even sophisticated single-moment BMPSs do not guarantee better results.
375 Furthermore, microphysics-focused studies tend to focus on strong convective events (i.e., squall lines, hurricanes,
376 etc.), yet provide little attention to strongly precipitating, stratiform-dominated events (such as nor'easters). Although
377 not conclusive, this study has shown that assumed precipitation tendencies may vary in light of the dominant
378 precipitation mode. Follow-on studies could investigate additional nor'easter cases or simulate other weather
379 phenomena (polar lows, monsoon rainfall, drizzle, etc). Results covering multiple phenomena may provide guidance
380 to model users in their selection of BMPS for a given computational cost. Additionally, potential studies could
381 specifically address key aspects of a nor'easter's structure (such as the low-level jet) or validation of model output
382 against current and recently available satellite-based datasets from MODIS (Justice et al., 2008), CloudSat (Stephens
383 et al., 2008), CERES, and GPM (Hou et al. 2014). Finally, other validation methods including object-oriented
384 (Marzban and Sandgathe, 2006) or fuzzy verification (Ebert 2008) could be utilized.

385 **5 Code availability**

386 WRF version 3.6.1 is publically available for download from the WRF Users' Page (http://www2.mmm.ucar.edu/wrf/users/download/get_sources.html).

388 **6 Data availability**

389 GFS model analysis data boundary condition data can be obtained from the NASA's open access, NOMADS
390 data server (<ftp://nomads.ncdc.noaa.gov/GFS/Grid3/>). Stage IV precipitation data is publically available from the
391 National Data and Software Facility at the University Center for Atmospheric Research (http://data.eol.ucar.edu/cgi-bin/codiac/fgr_form/id=21.093).

393 **7 Author contributions**

394 S. D. Nicholls designed and ran all experimental model simulations and prepared the manuscript. S. G. Decker
395 supervised S. D. Nicholls' research efforts, funded the research, and revised the manuscript. W. -K. Tao, S. E. Lang,
396 and J. J. Shi brought their extensive knowledge and expertise on model microphysics which helped shape the project



397 methodology and rationalize the results. Finally, K. I. Mohr helped to facilitate connections between the research
398 team, supervised S. Nicholls' research, and was pivotal in revising the manuscript.

399 **8 Acknowledgements**

400 This research was supported by the 2011 Graduate Student Summer Program (GSSP), the Joint Center for Earth
401 Systems Technology (JCET), the University of Maryland Baltimore County (UMBC), and in part by the New Jersey
402 Agricultural Experiment Station. Resources supporting this work were provided by the NASA High-End Computing
403 (HEC) Program through the NASA Center for Climate Simulation (NCCS) at Goddard Space Flight Center.

404 **References**

- 405 Ashton, A. D., Donnelly, J. P., and Evans, R. L.: A discussion of the potential impacts of climate change on the
406 shorelines of the Northeastern U.S.A. *Mitig. Adapt. Strat. Glob. Change*, 13, 719–743, 2008.
- 407 Bosart, L. F.: The Presidents' Day Snowstorm of 18–19 February 1979: A subsynoptic-scale event, *Mon. Wea. Rev.*,
408 109, 1542–1566, 1981.
- 409 Buizza, R., Houtekamer, P. L., Pellerin, G., Toth, Z., Zhu, Y., and Wei, M.: A comparison of the ECMWF, MSC,
410 and NCEP global ensemble prediction systems, *Mon. Wea. Rev.*, 133, 1076–1097, 2005
- 411 Chen, F., and Dudhia, J.: Coupling an advanced land-surface/ hydrology model with the Penn State/ NCAR MM5
412 modeling system. Part I: Model description and implementation, *Mon. Wea. Rev.*, 129, 569–585, 2001.
- 413 Chern, J. -D., Tao, W. -K., Lang, S. E., Matsui, T., J. -L. F. Li, J. -L. F., Mohr, K. I., Skofronick-Jackson, G. M.,
414 and Peters-Lidard, C. D.: Performance of the Goddard multiscale modeling framework with Goddard ice
415 microphysical schemes, *J. Adv. Model. Earth Syst.*, 7, doi:10.1002/2015MS000469, 2016.
- 416 Chou, M. -D. and Suarez, M. J.: A solar radiation parameterization for atmospheric research studies. NASA Tech,
417 Memo NASA/TM-1999-104606, 40 pp., 1999.
- 418 Chou, M. -D., and Suarez, M. J.: A thermal infrared radiation parameterization for atmospheric studies, NASA Tech.
419 Rep. NASA/TM-1999-10466, vol. 19, 55 pp., 2001.
- 420 Dravitzki, S., and McGregor, J.: Predictability of heavy precipitation in the Waikato River Basin of New
421 Zealand, *Mon. Wea. Rev.*, 139, 2184–2197, 2011.
- 422 Dudhia, J., Hong, S. -Y., and Lim, K. -S.: A new method for representing mixed-phase particle fall speeds in bulk
423 microphysics parameterizations, *J. Meteor. Soc. Japan*, 86A, 33–44, 2008.
- 424 Ebert, E. E.: Fuzzy verification of high-resolution gridded forecasts: A review and a proposed framework, *Meteor.*
425 *Applic.*, 15, 51-64, 2008.
- 426 Forbes, G. S., Thomson, D. W., and Anthes, R. A.: Synoptic and mesoscale aspects of an Appalachian ice storm
427 associated with cold-air damming, *Mon. Wea. Rev.*, 115, 564–591, 1987.
- 428 Fritsch, J. M., and Carbone, R. E.: Improving quantitative precipitation forecasts in the warm season: A USWRP
429 research and development strategy, *Bull. Amer. Meteor. Soc.*, 85, 955–965, 2004.



- 430 Ganetis, S. A. and Colle, B. A.: The thermodynamic and microphysical evolution of an intense snowband during the
 431 Northeast U.S. blizzard of 8–9 February 2013. *Mon. Wea. Rev.*, 143, 4104–4125, 2015.
- 432 Hong, S. -Y., and Lim, J. -O. J.: The WRF single-moment 6-class microphysics scheme (WSM6), *J. Korean Meteor.*
 433 *Soc.*, 42, 129–151, 2006.
- 434 Hong, S. -Y., Lim, K. -S. S., Lee, Y. -H., Ha, J. -C., Kim, H. -W., Ham, S. -J., and Dudhia, J.: Evaluation of the
 435 WRF double-moment 6-class microphysics scheme for precipitating convection, *Adv. Meteor.*, 2010,
 436 doi:10.1155/2010/707253, 2010.
- 437 Hou, A. Y., Kakar, R. K., Neeck, S., Azarbarzin, A. A., Kummerow, C. D., Kojima, M., Oki, R., Nakamura, K., and
 438 Iguchi, T.: The Global Precipitation Measurement Mission, *Bull. Amer. Meteor. Soc.*, 95, 701–722, 2014.
- 439 Jacobs, N. A., Lackmann, G. M., and Raman, S.: The combined effects of Gulf Stream-induced baroclinicity and
 440 upper-level vorticity on U.S. East Coast extratropical cyclogenesis, *Mon. Wea. Rev.*, 133, 2494–2501, 2005.
- 441 Janjic, Z. I.: Nonsingular implementation of the Mellor–Yamada level 2.5 scheme in the NCEP meso model, NCEP
 442 Office Note 437, 61 pp., 2002.
- 443 Justice, C. O. et al. (1998), The Moderate Resolution Imaging Spectroradiometer (MODIS): land remote sensing for
 444 global change research, *IEEE Transactions on Geoscience and Remote Sensing*, 36, 1228–1249, 1998.
- 445 Kain, J. S. (2004), The Kain–Fritsch Convective Parameterization: An Update, *J. Appl. Meteor.*, 43, 170–181, 2004.
- 446 Kessler, E. (1969), On the distribution and continuity of water substance in atmospheric circulation, *Meteor. Monogr.*,
 447 32, *Amer. Meteor. Soc.*, 84 pp, 1969.
- 448 Kim, H. M., and Jung, B. -J.: Influence of moist physics and norms on singular vectors for a tropical cyclone. *Mon.*
 449 *Wea. Rev.*, 137, 525–543, 2009.
- 450 Kocin, P. J. and Uccellini, L. W.: Northeast snowstorms. Vols. 1 and 2, *Meteor. Monogr.*, No. 54., *Amer. Met. Soc.*,
 451 818 pp., 2004.
- 452 Kuo, Y. H., Low-Nam, S., and Reed, R. J.: Effects of surface energy fluxes during the early development and rapid
 453 intensification stages of seven explosive cyclones in the Western Atlantic. *Mon. Wea. Rev.*, 119, 457–476, 1991.
- 454 Lang, S., Tao, W. -K., Cifelli, R., Olson, W., Halverson, J., Rutledge, S., and Simpson, J.: Improving simulations of
 455 convective system from TRMM LBA: Easterly and westerly regimes, *J. Atmos. Sci.*, 64, 1141–1164, 2007.
- 456 Lang, S. E., Tao, W. -K., Zeng, X., and Li, Y.: Reducing the biases in simulated radar reflectivities from a bulk
 457 microphysics scheme: Tropical convective systems, *J. Atmos. Sci.*, 68, 2306–2320, 2011.
- 458 Lang, S. E., Tao, W. -K., Chern, J. -D., Wu, D., and Li, X.: Benefits of a fourth ice class in the simulated radar
 459 reflectivities of convective systems using a bulk microphysics scheme, *J. Atmos. Sci.*, 71, 3583–3612,
 460 doi:10.1175/JAS-D-13-0330.1, 2014.
- 461 Lebsock, M., and Su, H: Application of active spaceborne remote sensing for understanding biases between passive
 462 cloud water path retrievals, *J. Geophys. Res. Atmos.*, 119, 8962–8979, doi:10.1002/2014JD021568, 2014.
- 463 Li, J. -L. F., Waliser, D., Woods, C., Teixeira, J., Bacmeister, J., Chern, J. -D., Shen, B. -W., Tompkins, A., Tao,
 464 W. -K., and Kohler, M.: Comparisons of satellites liquid water estimates to ECMWF and GMAO analyses,
 465 20th century IPCC AR4 climate simulations, and GCM simulations, *Geophys. Res. Lett.*, 35, L19710,
 466 doi:10.1029/2008GL035427, 2008.



- 467 Lim, K.-S. and Hong, S. -Y.: Development of an effective double-moment cloud microphysics scheme with
468 prognostic cloud condensation nuclei (CCN) for weather and climate models, *Mon. Wea. Rev.*, 138, 1587–
469 1612, 2010.
- 470 Lin, Y. -L., Farley, R. D., and Orville, H. D.: Bulk parameterization of the snow field in a cloud model, *J. Climate*
471 *Appl. Meteor.*, 22, 1065–1092, 1983.
- 472 Mailhot, J. and Chouinard, C.: Numerical forecasts of explosive winter storms: Sensitivity experiments with a meso-
473 scale model, *Mon Wea. Rev.*, 117, 1311–1343, 1989.
- 474 Marzban C., and Sandgathe, S.: Cluster analysis for verification of precipitation fields, *Wea. Forecasting*, 21, 824–
475 838, 2006.
- 476 Mellor, G. L., and Yamada, T.: Development of a turbulence closure model for geophysical fluid problems, *Rev.*
477 *Geophys. Space Phys.*, 20, 851–875, 1982.
- 478 Monin, A. S., and Obukhov, A. M.: Basic laws of turbulent mixing in the surface layer of the atmosphere. *Tr. Akad.*
479 *Nauk SSSR Geophys. Inst.*, 24, 163–187, 1954.
- 480 Morath, E. (2016), Will a blizzard freeze U.S. economic growth for the third straight year, *Wall Street Journal*, 20
481 Jan. 2016.
- 482 Morrison, H., Thompson, G., and Tatarskii, V.: Impact of cloud microphysics on the development of trailing stratiform
483 precipitation in a simulated squall line: Comparison of one- and two-moment schemes, *Mon. Wea. Rev.*, 137,
484 991–1007, 2009.
- 485 Mote, T. L., Gamble, D. W., Underwood, S. J., Bentley, M. L.: Synoptic-scale features common to heavy snowstorms
486 in the Southeast United States, *Wea. Forecasting*, 12, 5–23, 1997.
- 487 Nicholls, S. D. and Decker, S. G.: Impact of coupling an ocean model to WRF nor'easter simulations, *Mon. Wea.*
488 *Rev.*, 143, 4997–5016, 2015.
- 489 Reeves, H. D. and Dawson II, D. T.: The dependence of QPF on the choice of microphysical parameterization for
490 lake-effect snowstorms, *J. Appl. Meteor. Climatol.*, 52, 363–377, 2013.
- 491 Reisner, J. R., Rasmussen, R. M., and Bruintjes, R. T.: Explicit forecasting of supercooled liquid water in winter
492 storms using the MM5 mesoscale model. *Quar. J. Roy. Met. Soc.*, 124, 1071-1107, 1998.
- 493 Ridout, J. A., Y. Jin, and Liou, C. -S.: A cloud-base quasi-balance constraint for parameterized convection:
494 Application to the Kain–Fritsch cumulus scheme, *Mon. Wea. Rev.*, 133, 3315–3334, 2005.
- 495 Rutledge, S. A., and Hobbs, P. V.: The mesoscale and microscale structure and organization of clouds and precipitation
496 in midlatitude cyclones. XII: A diagnostic modeling study of precipitation development in narrow cloud-frontal
497 rainbands. *J. Atmos. Sci.*, 20, 2949–2972, 1984.
- 498 Serreze, M. C.: Climatological aspects of cyclone development and decay in the Arctic, *Atmos.-Ocean*, 33, 1–23,
499 1995.
- 500 Serreze, M. C., Carse, F., Barry, R. G., and Rogers, J. C.: Icelandic low cyclone activity: Climatological features,
501 linkages with the NAO and relationships with recent changes in the Northern Hemisphere circulation, *J. Climate*,
502 10, 453–464, 1997.



- 503 Shi, J. J. et al.: WRF simulations of the 20-22 January 2007 snow events of Eastern Canada: Comparison with in situ
 504 and satellite observations, *J. Appl. Meteor. Climatol.*, 49, 2246–2266, 2010.
- 505 Skamarock, W. C., Klemp, J. P., Dudhia, J., Gill, D. O., Barker, D. M., Duda, M. G., Huang, X. -Y., Wang, W., and
 506 Powers, J. G.: A description of the advanced research WRF version 3, NCAR Tech. Note NCAR/TN-475+STR,
 507 125 pp., 2008.
- 508 Smith, A. B., and Katz, R. W.: US billion-dollar weather and climate disasters: Data sources, trends, accuracy and
 509 biases, *Natural Hazards*, 67, 387–410, 2013.
- 510 Stark, D.: Field observations and modeling of the microphysics within winter storms over Long Island, NY. M.S.
 511 thesis, School of Marine and Atmospheric Sciences, Stony Brook University, 132 pp., 2012.
- 512 Stauffer, D. R., and Warner, T. T.: A numerical study of Appalachian cold-air damming and coastal frontogenesis,
 513 *Mon. Wea. Rev.*, 115, 799–821, 1987.
- 514 Stephens, G. L., et al.: CloudSat mission: Performance and early science after the first year of operation, *J. Geophys.*
 515 *Res.*, 113, D00A18, doi:10.1029/2008JD009982, 2008.
- 516 Stith, J. L., Dye, J. E., Bansemer, A., Heymsfield, A. J., Grainger, C. A., Petersen, W. A., and Clifelli, R.:
 517 Microphysical observations of tropical clouds, *J. Appl. Meteor.*, 41, 97–117, 2002.
- 518 Tao, W. -K., Simpson, J. and McCumber, M.: An ice-water saturation adjustment, *Mon. Wea. Rev.*, 117, 231–235,
 519 1989.
- 520 Tao, W. -K., Shi, J. J., Chen, S. S., Lang, S., Lin, P. -L., Hong, S. -Y., Peters-Lidard, C., and Hou, A.: The impact of
 521 microphysical schemes on hurricane intensity and track, *Asia-Pacific J. Atmos. Sci.*, 47, 1–16, 2011.
- 522 Tao, W. -K., Wu, D., Lang, S., Chern, J. -D., Peters-Lidard, C., Fridlind, A., and Matsui, T.: High-resolution NU-
 523 WRF simulations of a deep convective-precipitation system during MC3E: Further improvements and
 524 comparisons between Goddard microphysics schemes and observations, *J. Geophys. Res. Atmos.*, 121, 1278–
 525 1305, doi:10.1002/2015JD023986, 2016.
- 526 Uccellini, L. W. and Kocin, P. J.: The Interaction of jet streak circulations during heavy snow events along the east
 527 coast of the United States, *Wea. Forecasting*, 2, 289–308, 1987.
- 528 Wang, S.-Y., and Clark, A. J.: NAM Model forecasts of warm-season quasi-stationary frontal environments in the
 529 Central United States, *Wea. Forecasting*, 25, 1281–1292, 2010.
- 530 Wilks, D. S.: Statistical methods in the atmospheric sciences, third edition, Academic Press, Oxford, in press., 2011.
- 531 Wu, L., and Petty, G. W.: Intercomparison of bulk microphysics schemes in model simulations of polar lows, *Mon.*
 532 *Wea. Rev.*, 138, 2211–2228, 2010.
- 533 Yao, Y., Pierre, W., Zhang, W., and Jiang, J.: Characteristics of atmosphere-ocean interactions along North Atlantic
 534 extratropical storm tracks, *J. Geophys. Res.*, 113, doi:10.1029/2007JD008854, 2008.



535 **Table 1.** Nor'easter case list. The NESIS number is included for storm severity reference. The last two columns denote
 536 the first and last times for each model run. Tracks are plotted in Fig. 2.
 537

Case Number	NESIS	Event Dates	Model Run Start Date	Model Run End Date
1	N/A	15–16 Oct 2009	10/12 12UTC	10/20 00UTC
2	N/A	07–09 Nov 2012	11/04 06UTC	11/11 18UTC
3	4.03	19–20 Dec 2009	12/16 06UTC	12/23 18UTC
4	2.62	26–28 Jan 2015	01/23 00UTC	01/30 12 UTC
5	4.38	04–07 Feb 2010	02/02 18UTC	02/10 06UTC
6	1.65	01–02 Mar 2009	02/26 12UTC	03/06 00UTC
7	N/A	12–14 Mar 2010	03/09 06UTC	03/16 18UTC

538



539 **Table 2.** Applied bulk microphysics schemes and their characteristics. The below table indicates simulated mixing
 540 ratio species and number of moments. Mixing ratio species include: QV = water vapor, QC = cloud water, QH = hail,
 541 QI = cloud ice, QG = graupel, QR = rain, QS = snow.

Microphysics Scheme	QV	QC	QH	QI	QG	QR	QS	Moments	Citation
Lin6	X	X		X	X	X	X	1	Lin et al. (1983); Rutledge and Hobbs (1984)
GCE6	X	X		X	X	X	X	1	Tao et al. (1989); Lang et al. (2007)
GCE7	X	X	X	X	X	X	X	1	Lang et al. (2014)
WSM6	X	X		X	X	X	X	1	Hong and Lim (2006)
WDM6	X	X		X	X	X	X	2 (QC, QR)	Lim and Hong (2010)

542



543 **Table 3.** Various simulated nor'easter characteristics. Bolded values indicate sea-level pressure values or rate errors
 544 > 5 hPa (/6 hours), wind errors > 5 m s⁻¹, and average track errors > 400 km.

<i>GMA</i>	1	2	3	4	5	6	7
Min SLP (hPa)	991.5	989.5	972.6	980.5	979.7	1000.5	993.5
Max SLP decrease (hPa/6hrs)	-6.0	-5.9	-6.4	-10.8	-7.9	-3.2	-2.7
Max 10 m Wind (m s ⁻¹)	24.4	24.8	23.4	22.9	23.1	16.4	15.2
<i>Lin6</i>	1	2	3	4	5	6	7
Min SLP (hPa)	995.2	982.8	983.1	989.8	978.2	1001.9	998.1
Max SLP decrease (hPa/6hrs)	-4.1	-6.0	-6.9	-5.5	-6.4	-3.3	-2.7
Max 10 m Wind (m s ⁻¹)	24.1	20.0	30.6	26.2	23.3	14.2	26.4
Avg Track Error (km)	505	767	356	131	490	219	404
<i>GCE6</i>	1	2	3	4	5	6	7
Min SLP (hPa)	990.0	982.2	976.7	988.0	981.7	1002.2	996.4
Max SLP decrease (hPa/6hrs)	-8.5	-6.7	-9.0	-6.0	-6.2	-3.5	-3.9
Max 10 m Wind (m s ⁻¹)	28.7	18.1	33.0	22.1	23.5	15.5	23.5
Avg Track Error (km)	366	789	311	140	465	197	576
<i>GCE7</i>	1	2	3	4	5	6	7
Min SLP (hPa)	989.0	983.1	976.9	987.3	976.2	1002.1	996.3
Max SLP decrease (hPa/6hrs)	-4.3	-7.2	-9.8	-6.0	-6.4	-3.2	-3.7
Max 10 m Wind (m s ⁻¹)	24.3	19.1	30.2	20.6	23.0	16.1	24.6
Avg Track Error (km)	445	792	317	129	479	225	541
<i>WSM6</i>	1	2	3	4	5	6	7
Min SLP (hPa)	996.0	982.3	978.6	989.3	976.2	1002.5	996.3
Max SLP decrease (hPa/6hrs)	-3.9	-5.9	-8.9	-5.3	-5.2	-3.2	-6.1
Max 10 m Wind (m s ⁻¹)	22.1	17.7	25.6	24.4	21.5	21.1	21.5
Avg Track Error (km)	553	789	327	140	518	233	544
<i>WDM6</i>	1	2	3	4	5	6	7
Min SLP (hPa)	992.7	980.9	977.1	988.6	978.5	1001.4	995.0
Max SLP decrease (hPa/6hrs)	-4.9	-6.5	-8.7	-5.5	-8.7	-2.7	-5.8
Max 10 m Wind (m s ⁻¹)	23.1	19.6	33.2	20.4	23.2	15.9	23.4
Avg Track Error (km)	543	804	333	138	567	219	452



545 **Table 4.** Stage IV-relative, storm-total precipitation threat scores and biases assuming a threshold value of 12.5 mm
 546 (0.5"). Bolded value denote the model simulation with the threat score closest to 1 (perfect forecast) and bias values
 547 closest to 1 (no precipitation bias).

<i>Threat Score</i>	1	2	3	4	5	6	7	Mean
Lin6	0.40	0.16	0.25	0.40	0.58	0.57	0.31	0.38
GCE6	0.41	0.17	0.23	0.34	0.54	0.57	0.31	0.37
GCE7	0.40	0.17	0.23	0.35	0.56	0.56	0.29	0.37
WSM6	0.39	0.16	0.23	0.35	0.55	0.57	0.30	0.36
WDM6	0.39	0.16	0.23	0.36	0.58	0.59	0.31	0.37

<i>Bias</i>	1	2	3	4	5	6	7	Mean
Lin6	1.38	4.62	0.71	1.79	1.34	1.33	1.12	1.76
GCE6	1.34	4.52	0.81	2.10	1.45	1.33	1.12	1.81
GCE7	1.40	4.50	0.85	2.04	1.40	1.35	1.20	1.82
WSM6	1.45	4.72	0.81	2.07	1.44	1.33	1.14	1.85
WDM6	1.45	4.68	0.82	2.01	1.36	1.30	1.10	1.82

548



549 **Table 5.** Energy norm analysis for model- and GMA-relative cyclone locations. Energy norm values are derived from
 550 domain 2 data and only within a 600-km diameter box centered on the model-indicated cyclone location. “Per case
 551 rank order” ranks the models based upon number of instances of lowest model error for each of the seven cases and
 552 allows for ties.
 553

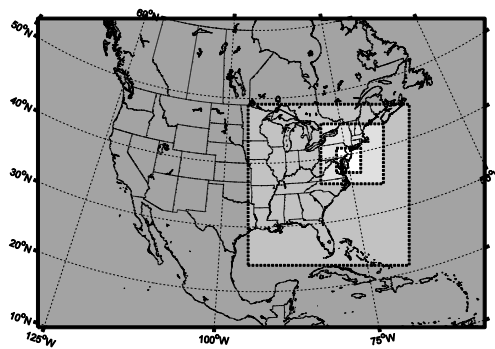
Model-Relative Energy Norm Analysis

Total 62 Periods	Lin6	GCE6	GCE7	WSM6	WDM6
Lowest Energy Norm (% of total)	18 (29.0 %)	8 (12.9 %)	8 (12.9 %)	15 (24.2 %)	13 (21.0 %)
Avg Δ ENorm vs. Lin6 (% of Lin Enorm)	N/A	3.23E+5 (5.73 %)	8.75E+4 (1.55 %)	1.85E+4 (0.33 %)	3.72E+5 (6.59 %)
2-Tailed P-Value (vs Lin6)	N/A	0.406	0.11	0.941	0.652
Per Case Rank Order (of 5)	2113312	4223334	2423154	1233223	4521211

GMA-Relative Energy Norm Analysis

Total: 67 Periods	Lin6	GCE6	GCE7	WSM6	WDM6
Lowest Energy Norm	24 (35.8 %)	5 (7.5 %)	6 (9.0 %)	17 (25.4 %)	15 (22.4 %)
Avg Δ ENorm vs. Lin6 (% of Lin Enorm)	N/A	2.69E+5 (6.16 %)	2.61E+5 (5.97 %)	1.54E+4 (0.35 %)	-1.14E+5 (- 2.58 %)
2-Tailed P-Value (vs Lin6)	N/A	0.414	0.24	0.882	0.589
Per Case Rank Order (of 5)	2221121	3454242	3414545	1141224	3233212

554

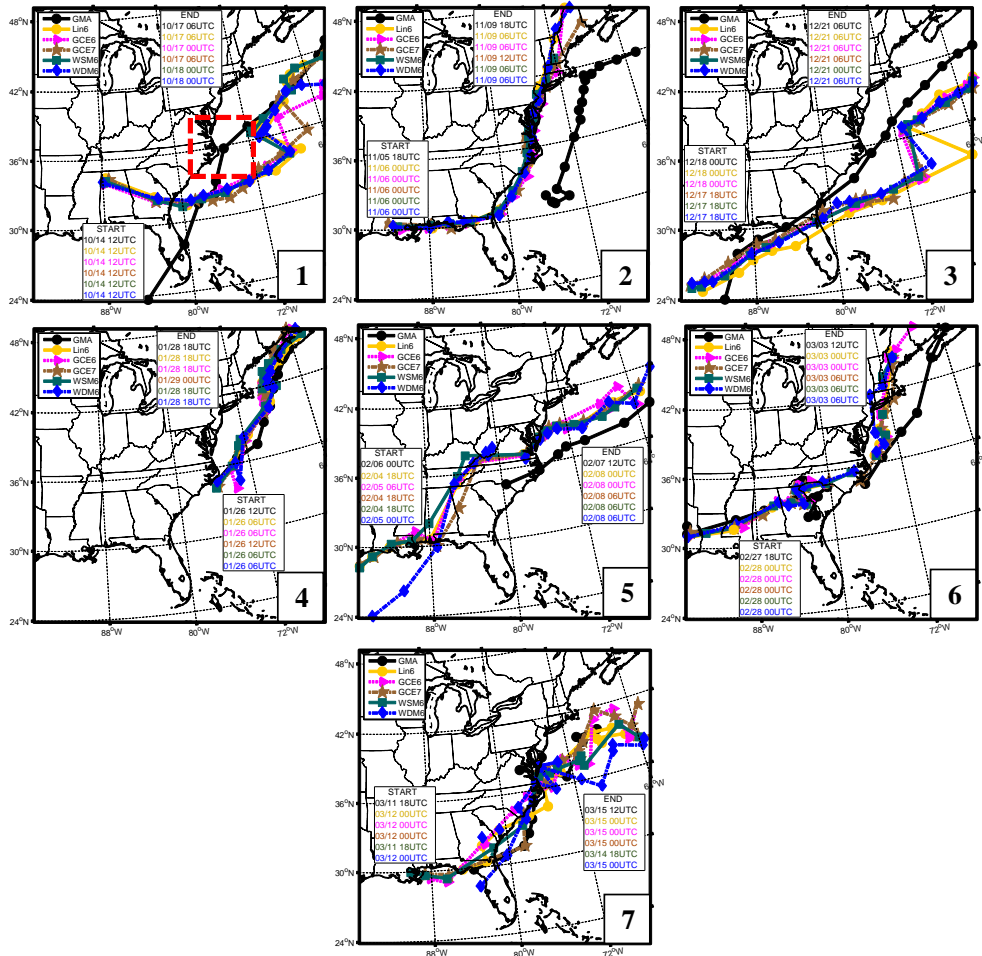


555

556 **Figure 1.** Nested WRF configuration used in simulations. Horizontal resolution for domains 1, 2, 3, and 4 are
557 15, 5, and 1.667 km, respectively.



558
 559
 560
 561
 562
 563
 564
 565
 566
 567
 568
 569
 570
 571
 572
 573
 574
 575
 576
 577
 578
 579
 580
 581
 582



583 **Figure 2.** Storm tracks from GMA and the model runs. Line legend is shown on the upper-left of each plot. Shown
 584 symbols indicate simulated storm position every six hours. Black numbers indicate case number. The red, dashed
 585 box in case 1, shows the size of a 600-km diameter box.



586
587
588
589
590
591
592
593
594
595
596
597
598
599
600
601
602
603
604
605
606
607
608
609

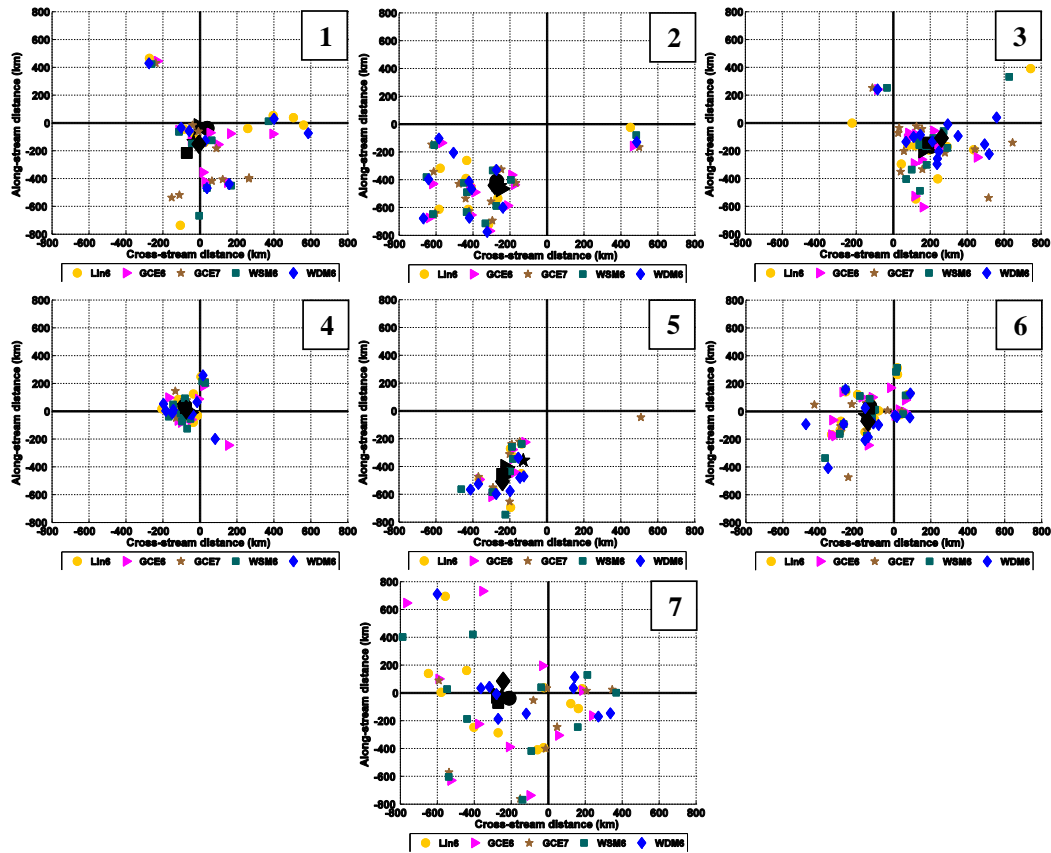
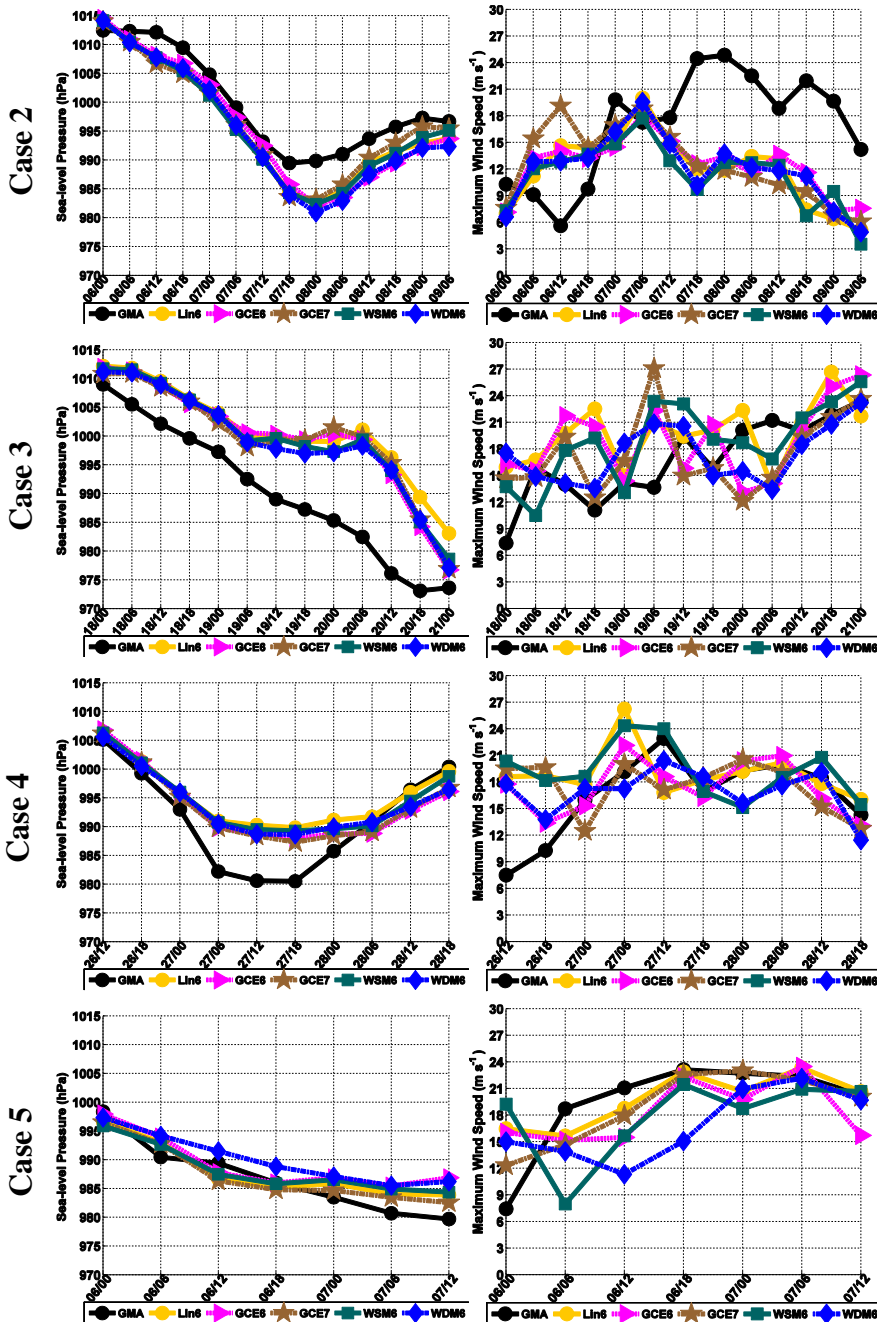


Figure 3. GMA-relative storm track error (km). Smaller, colored symbols denote storm track error every six hours and the large, black symbols denote the model mean error. The positive y-axis is aligned to six-hourly, GMA-relative storm track propagation direction. Black numbers indicate case number.



610

Minimum Sea-level Pressure (hPa) Maximum surface wind (m s^{-1})



611

612

613

614

615

616

Figure 4. Plots of storm minimum sea-level pressure (hPa, left-hand panels) and maximum surface wind speed (m s^{-1}) within 600 km of the cyclone center from cases 2, 3, 4, and 5.

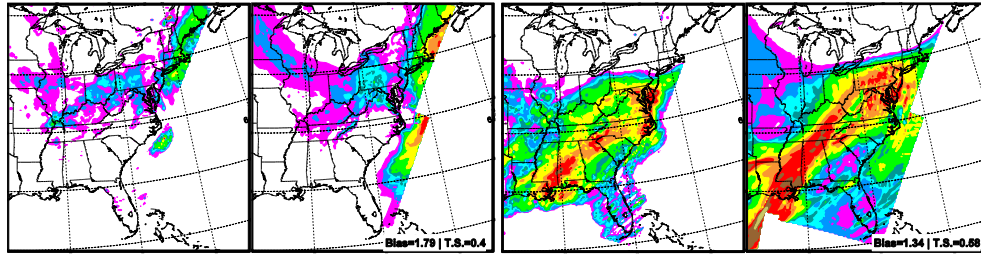


617

Case 4

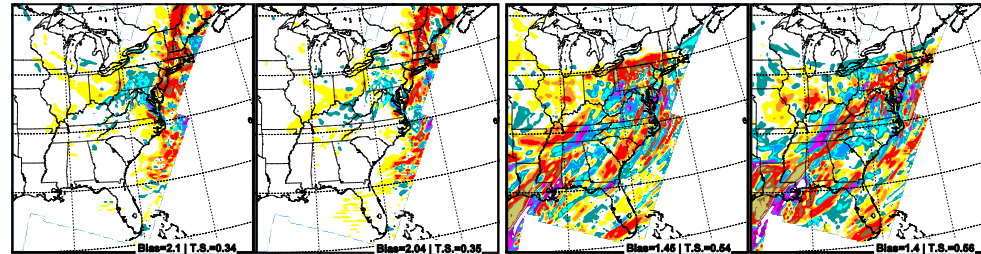
Case 6

Stage IV & Lin6

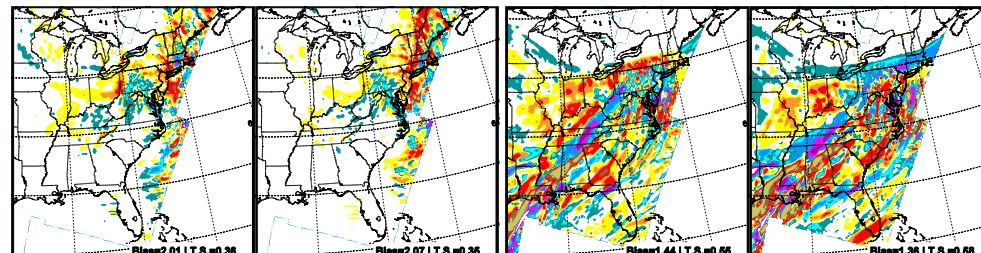


619

GCE6 & GCE7

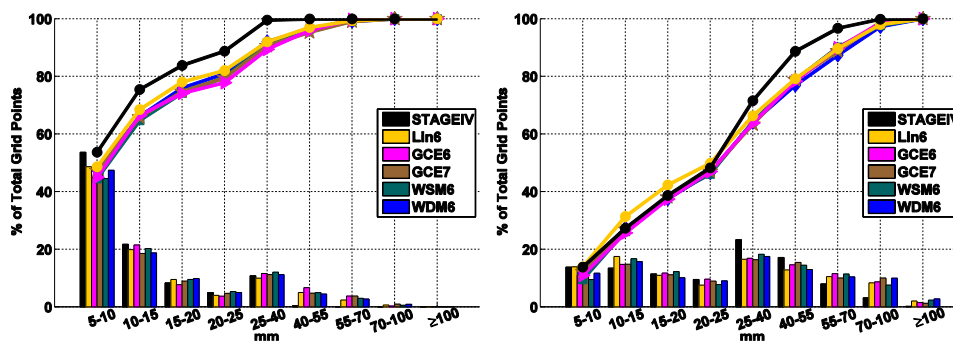


WSM6 & WDM6



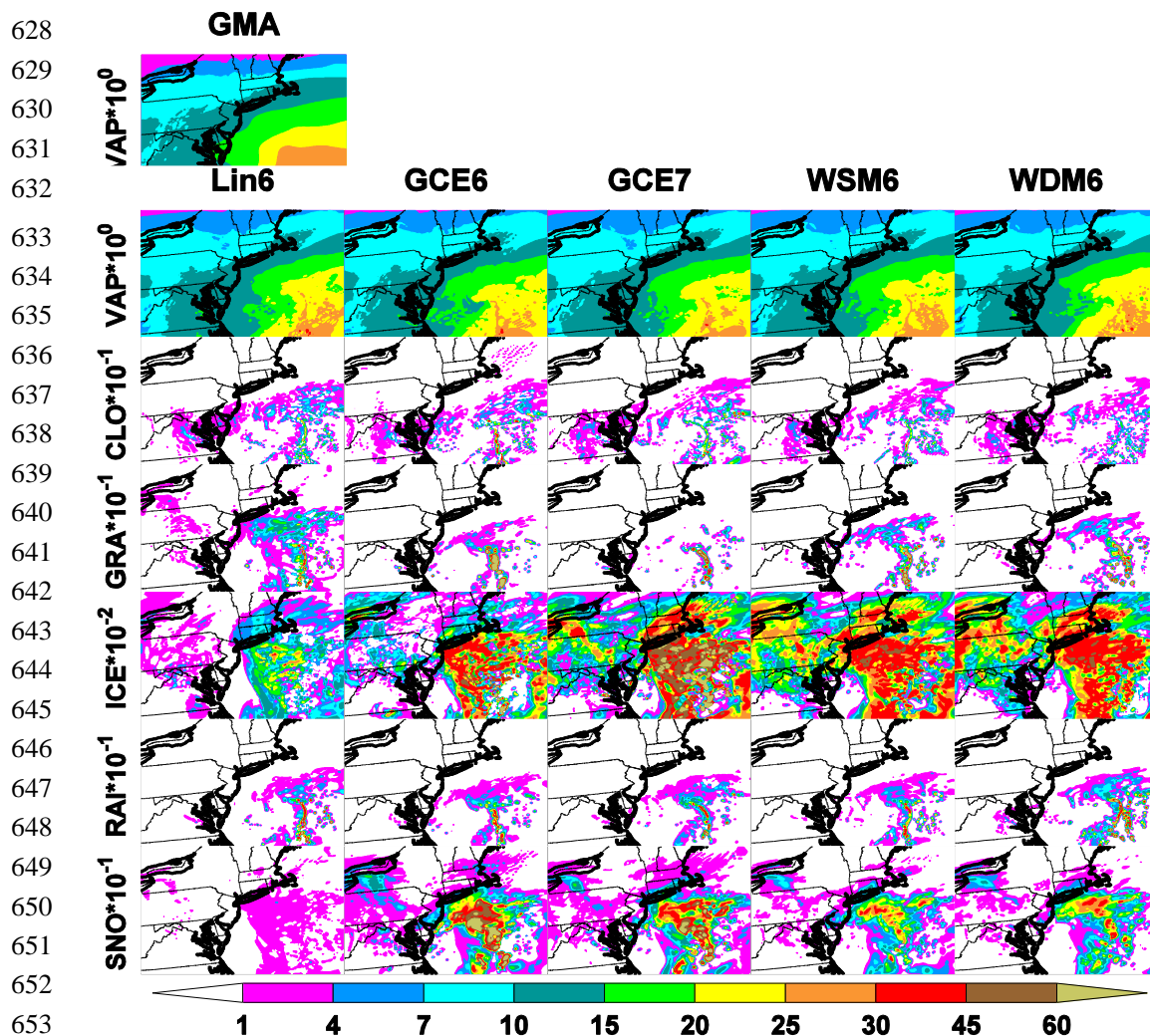
622

Precip. PDF/CDF



623

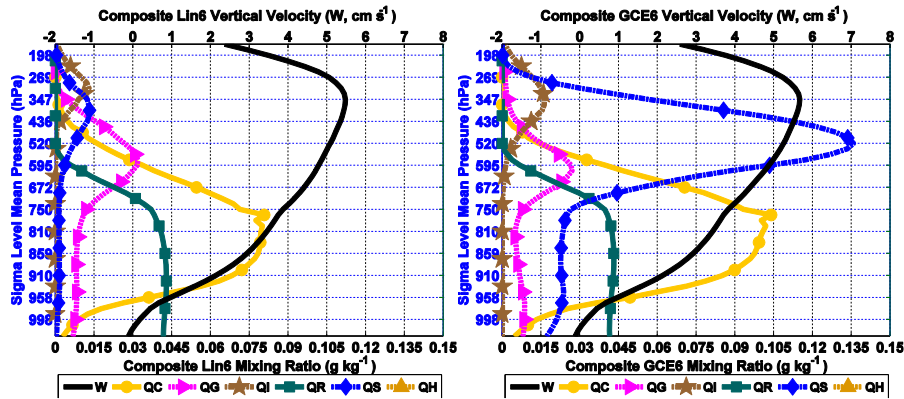
624 **Figure 5.** (top) 72-hour total precipitation accumulation (mm; forecast hours 48–120) from Stage IV and Lin6.
 625 (middle) Difference between other models and Lin6 (mm, model-Lin6). (bottom) Probability density and cumulative
 626 distribution functions of 72-hour accumulated precipitation for Stage IV and all models. Left-hand panels are for Case
 627 4 and right-hand panels are for Case 6.



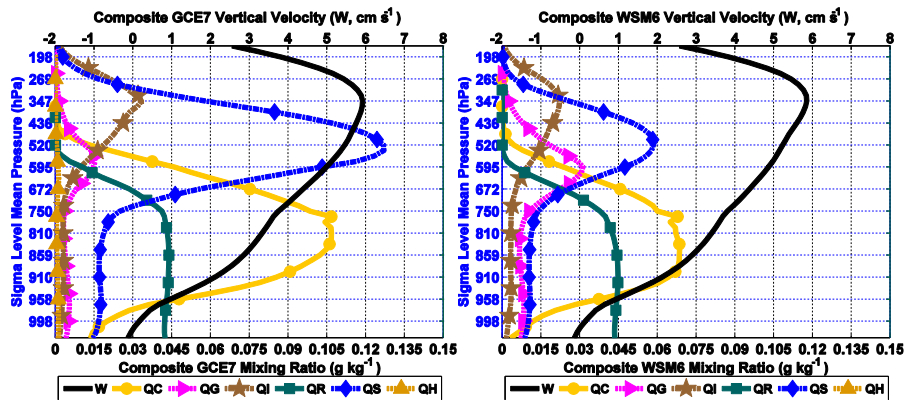
654 **Figure 6.** Domain 3, precipitable mixing ratios (mm) at 18 UTC 26 Jan 2015. Shown abbreviations for mixing ratios
 655 include: VAP = water vapor, CLO = cloud water, GRA = graupel, ICE = cloud ice, RAI = rain, SNO = snow.



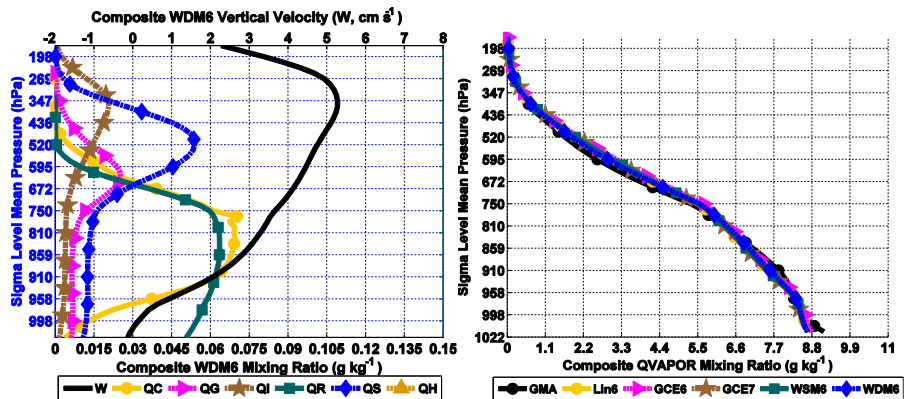
656



657



658



659 **Figure 7.** Composite mixing ratios (g kg^{-1}) and vertical velocities (cm s^{-1}) averaged over at all model-relative storm
 660 track locations (within 600 km diameter box) and all seven nor'easter cases. Mixing ratio species abbreviations are QC
 661 (cloud water), QG (graupel), QI (cloud ice), QR (rain), QS (snow) and QH (hail), and QVAPOR (water vapor, lower-
 662 right panel only).



665

666

667

668

671

672

673

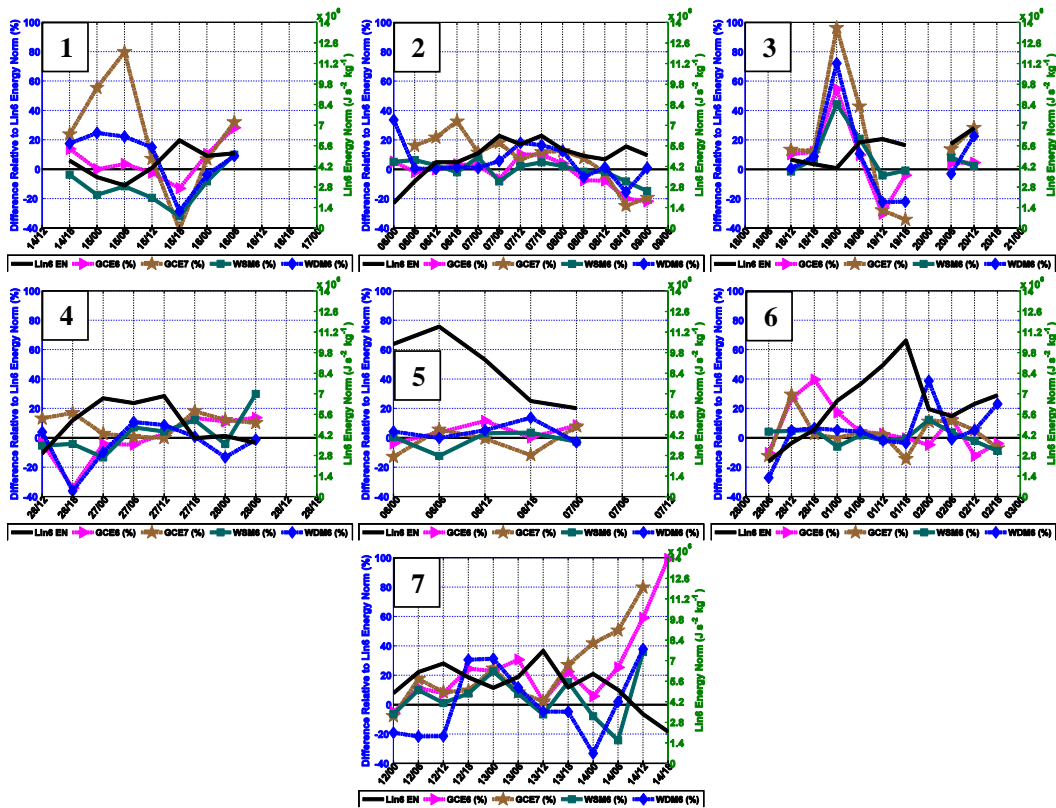
674

675

676

677

678



679

680

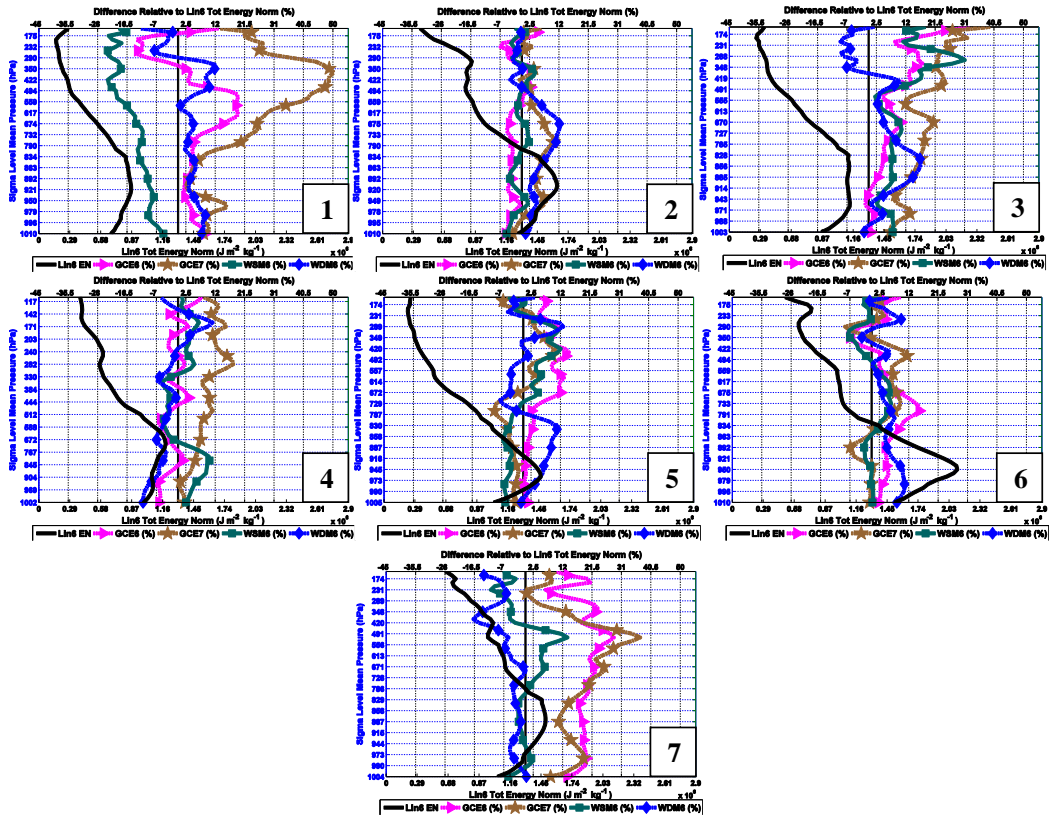
681

682

Figure 8. Model-relative total energy norm every six hours for each storm from Lin6 (black line, right y-axis) and difference (in percent) between energy norm from all other runs and Lin6 (colored lines, left y-axis). All energy norms were integrated only within a 600-km diameter box centered at the model indicated surface cyclone location. Positive percentage values indicate higher energy norm values than Lin6.



683
 684
 685
 686
 687
 688
 689
 690
 691
 692
 693
 694
 695
 696
 697
 698
 699



700 **Figure 9.** Model-relative total energy norm integrated on each model level and averaged over all times from Lin6
 701 (black line, bottom x-axis) and difference (in percent) between energy norm from all other runs and Lin6 (colored
 702 lines, top x-axis). All energy norms were integrated only within a 600-km diameter box centered at the model
 703 indicated surface cyclone location. Postive percentage values indicate higher energy norm values than Lin6.



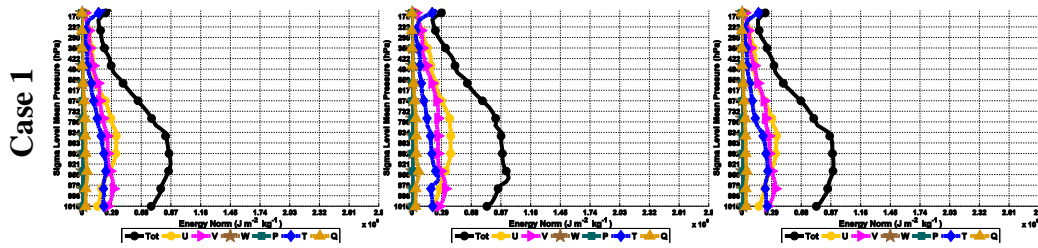
704

Lin6

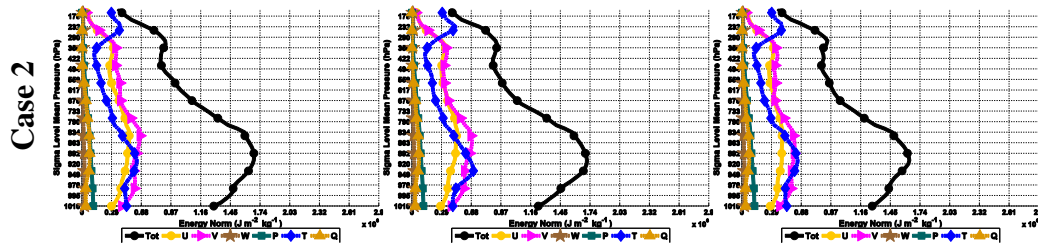
GCE7

WDM6

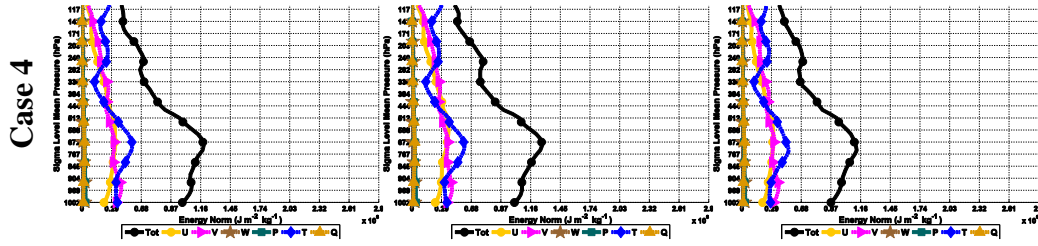
705



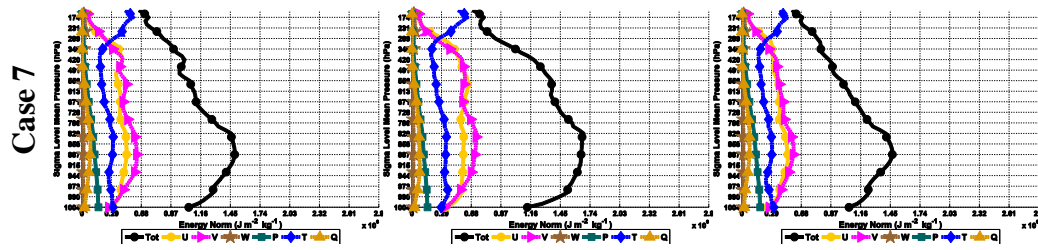
706



707



708



709 **Figure 10.** Time-averaged, model-relative storm environment energy norm components for cases 1, 2, 4, and 7 from
 710 the Lin6, GCE7, and WDM6 simulations. Shown lines include total energy norm (Tot; black) and its six-components
 711 (colors) including zonal wind (U; yellow), meridional wind (V; pink), vertical velocity (W; brown), atmospheric
 712 pressure (P; green), temperature (T, blue), and mixing ratio (Q; gold).